Active and passive seismic imaging of the central Abitibi greenstone belt, Larder Lake, Ontario

Mostafa Naghizadeh[1], Richard Smith[1], Kate Rubingh[1], Ross Sherlock[1], John Ayer[1], Bruno Lafrance[1], Saeid Cheraghi[1], David Snyder[1], Jérome Vergne[2], Dan Hollis[2], and Aurélien Mordret[2]

[1]Mineral Exploration Research Centre, Harquail School of Earth Sciences, Laurentian University, 935 Ramsey Lake Rd, Sudbury, Ontario, Canada P3E 2C6

[2]Sisprobe, IMAG building, 700 avenue Centrale, 38401 Saint Martin d'Hères, France

Plain Language Summary

It is becoming increasingly important to conduct mineral exploration projects in an environmental-friendly manner with minimal footprints left behind on the natural landscapes. The active source seismic reflection methods are considered the most accurate subsurface imaging geophysical prospecting methods, however, they often have high acquisition costs and might cause significant alterations to the environment. The passive seismic methods that utilize natural seismic sources can overcome most of these challenges. However, benchmark studies are still required to validate the effectiveness and accuracy of the images produced by passive seismic methods. We have conducted such a study by acquiring active and passive seismic surveys along an approximately 40 km transect in a world-class gold mineralization zone in Larder Lake, Ontario, Canada. The acquired passive seismic records were processed using the ambient noise surface wave tomography (ANSWT) and receiver function analysis methods to generate the shear-wave velocity and P- to S-wave (P-S) convertibility profiles of the subsurface, respectively. The good correlation between the active and passive seismic results indicated that the properly designed passive seismic surveys can be used as

alternatives to active seismic surveys leading to cheaper acquisition costs and fewer disturbances to the environment and nature.

Abstract

Passive seismic methods are considered as cost-effective and environmental-friendly alternatives to active (reflection) seismic methods. We have acquired co-located active and passive seismic surveys over a metal-endowed Archean granite-greenstone terrane in the Larder Lake area to investigate the reliability of the estimated elastic properties using the passive seismic methods. The passive seismic data was processed using two different data processing approaches, the ambient noise surface wave tomography (ANSWT) and receiver function analysis methods to generate shear-wave velocity and P- to S-wave (P-S) convertibility profiles of the subsurface, respectively. The Cadillac-Larder Lake Fault (CLLF) was imaged as a south-dipping sub-vertical zone of weak reflectivity in the reflection seismic profile. To the north of the CLLF, a package of north-dipping reflections in the upper-crust (at depths of 5-10 km) resides on the boundary of high (on the top) and low (on the bottom) shear-wave velocity zones estimated using the ANSWT method. This package of reflections is most likely caused by overlaying mafic volcanic and underlying felsic intrusive rocks. The P-S convertibility profile imaged the Moho boundary at ~40 km depth as well as a south-dipping slab that penetrates into the mantel which was interpreted to be either caused by the delamination of the lower crust or a possible deeper extension of the Porcupine-Destor Fault. Overall, the reflectivity, shear-wave velocity,

and P-S convertibility profiles exhibited a good correlation and provided a detailed image of the subsurface lithological structure to a depth of 10 km.

Keywords: Seismic Reflection, Passive Seismic, Ambient Noise Tomography, Receiver Functions, Archean Geology, Greenstone Belts

1. Introduction

The seismic reflection method is considered to be one of the most accurate depth-resolving geophysical prospecting method. A man-made/active source of seismic energy, vibroseis or explosives, propagates into the subsurface and the reflected seismic energy is recorded by an array of geophones. The collected data is then processed to generate a section that gives an indication of the subsurface acoustic impedance variations. The ME321-R1 seismic reflection transect, acquired as part of the Metal Earth project in 2017, is an approximately 44 km long transect that covers the Larder Lake area extending in a south-north orientation. Previously, the Lithoprobe project (Clowes et al., 1992) also acquired several reflection seismic profiles in the Central Abitibi area in close proximity to the Larder Lake area. Together, these transects can provide vital information about the reflectivity structure and tectonic evolution of the central Abitibi.

The logistical and economical burdens of using active seismic sources for the seismic reflection method are prohibitive factors for its wide-spread application. Therefore, a new class of seismic imaging methods that utilizes natural seismic sources (passive sources) has been experimented with to image the subsurface structures. One of these methods is the ambient noise surface wave tomography (ANSWT) method, that uses the correlations of seismic ambient noise recorded at two

stations to extract subsurface information (Campillo, 2006). By deploying an array of seismometers and recording the ambient noise for an extended period of time, the surface waves dispersion curves can be estimated and inverted to produce a subsurface shear-wave velocity model. One can also use the recorded data from the same array to isolate the signals from large teleseismic events and apply receiver function (RF) analysis to estimate the P- to S-wave (P-S) convertibility models (Ammon, 1991).

The Abitibi Greenstone Belt (AGB), the largest greenstone belt in the Archean Superior Province, extends from west of Timmins in Ontario to east of Chibougamau in Quebec (Figure 1a). This belt is composed of multiple cycles of volcanic and sedimentary rocks with very low-grade metamorphism that have been intruded by ultramafic to felsic rocks (Powell et al., 1995). Two different hypothesis have been proposed about the formation of the Superior province. One hypothesis asserts that the superior province is a collection of micro-continents and subduction-related arcs similar to the modern day plate tectonics processes (Calvert et al., 1995; White et al., 2003; Percival et al., 2006). However, another point of view prefers an Ensialic process with little horizontal movement that is driven by continental rifts zones (Bédard and Harris, 2014; Bédard, 2018). Whether contemporary plate tectonics processes were active in the Archean eon is a controversial topic (Van Kranendonk et al., 2004; Van-Hunen and Moyen, 2012). Geophysical investigations can play an important role in understanding and resolving these conflicting point of views about the tectonics and geodynamic setting of the Superior province.

In this paper, we have used seismic reflection profiles from the Metal Earth and Lithoprobe projects to study the crustal features in the Larder Lake area. We have also gathered and processed a passive seismic survey along the Metal Earth's ME321-R1 seismic reflection profile. The shear-wave

velocity and P- to S-wave convertibility models were estimated from passive seismic surveys using the ANSWT and RF analysis methods, respectively. The reflection seismic transects and estimated subsurface models from the passive seismic data were integrated with the magnetic and Bouguer gravity anomaly maps and the surface lithology in an attempt to attain reliable interpretation of geophysical anomalies.

2. Geology of the Abitibi Greenstone Belt

The Superior Province of Canada is the largest preserved Archean crust in the world. It contains a vast record of crustal growth from 3.22 Ga till 2.69 Ga (White et al., 2003) and comprises east-west trending granitoid, metasedimentary, and greenstone (metavolcanic) subprovinces. The Abitibi Greenstone Belt (ABG) is located in the eastern part of the Wawa-Abitibi subprovince of the Superior province (Figure 1a). Most of the volcanic and sedimentary units in the AGB are vertically dipping and can often be separated by east-trending faults with variable dip. Some of these faults, such as the Cadillac-Larder Lake Fault (CLLF), show signs of overprinting deformation events including early thrusting, as well as later strike-slip and extension events.

The southern Abitibi subprovince comprises six major volcanic assemblages, including from oldest to youngest: Pacaud (2750–2735 Ma), Deloro (2730–2724 Ma), Stoughton-Roquemaure (2723–2720 Ma), Kidd-Munro (2719–2711 Ma), Tisdale (2710–2704 Ma), and Blake River (2704–2696 Ma) (Ayer et al., 2005). Of these assemblages, two are present in the Larder Lake area: the Blake River and Tisdale. The lower part only of the Tisdale assemblage is present and is locally named the Larder Lake group (Figure 1b). The Blake River group consists dominantly of tholeiitic mafic volcanic and felsic volcanic units while the Larder Lake group is characterized by komatiitic ultramafic and tholeiitic mafic volcanic rocks. Although not recognized in the Larder Lake area, the

lower Tisdale assemblage locally contains units of calc-alkaline felsic volcanic rocks and banded iron formation (Ayer et al., 2005). These volcanic assemblages were intruded by calc-alkaline to alkaline composite stocks, ranging in age from ca. 2695 Ma to 2660 Ma, and were unconformably overlain by Porcupine turbidite-dominated sedimentary successions (2690–2685 Ma) and Timiskaming-type clastic-dominated sedimentary successions (<2677 – 2670 Ma) (Hyde, 1980; Corfu et al., 1991; Mueller et al., 1994; Powell et al., 1995; Davis et al., 2000; Ayer et al., 2002, 2005; Thurston et al., 2008).

The lithological map of the AGB near the Larder Lake area is shown in Figure 1a (Montsion et al., 2018). The yellow and green units are the felsic to ultramafic metavolcanics of the greenstone belt, with the successor basins shown in gray (early) and orange (late). The location of two major faults, CLLF and Porcupine-Destor Fault (PDF), are marked with blue dashed lines stretching predominantly in east-west directions. Figure 1b shows the corresponding assemblage map of the lithological units in Figure 1a. The assemblage map can play an important role in the interpretation of the seismic sections as it distinguishes the lithological units based on their age.

Figures 2a and 2b show the magnetic and Bouguer gravity anomalies for the same areal extent as Figure 1a, respectively. The magnetic data is collected by the Ontario government and has a relatively high resolution with a line spacing of 40 m. The gravity data is compiled by the Canadian government, primarily from measurement locations at spacing of up to 15 km which leads to relatively low-resolution image. The magnetic and gravity anomalies show features and contrasts at subprovince borders and the edges of large volcanic assemblages such as the Blake River group. The Metal-Earth Larder Lake transect ME321-R1 (shown by the white dashed line in Figures 2a and 2b)

is located on an area with a relatively high gravity and in a subdued area of the magnetic image; there are a few high magnetic anomalies across the transect, mostly related to mafic intrusions.

The upper crust in the Abitibi subprovince is composed of oceanic supracrustal assemblages and the middle crust has granitic and gneissic rocks. The greenstone belt upper crust often contains sub-vertical structures and low reflectivity, while the middle crust shows moderate to shallowly dipping structures and strong reflectivity in reflection seismic transects. According to Jackson et al. (1995) these structures could be interpreted to be the product of accretion of oceanic assemblages followed by extensive mid-crustal magmatism related to southward migration of an arc-trench system. In this interpretation, strong mid-crustal reflectivity is due to the ductile flow caused by thermal softening of the middle crust during magmatism. Also, the upward heat flow following magmatism caused late-tectonic low-pressure metamorphism in the upper crust (Jackson and Cruden, 1995).

3. Active Reflection Seismic Transects

Seismic line ME321-R1, which is approximately 40 km long, was acquired along a crooked profile (Figure 1a) across mafic/felsic meta-volcanic and meta-sedimentary units of the Abitibi greenstone belt. The profile crosses the CLLF shear zone and the Lincoln-Nipissing Fault (LNF), about 10 km to the south. Single wireless SG-5 vertical-component 5-Hz geophones with nominal receiver spacing of 25 meters were deployed along the profile. An array of four vibroseis trucks were used to produce a linear up-sweep of 2–96 Hz with a nominal source spacing of 12.5 m (Naghizadeh et al., 2019). The entire array of receivers were alive during the data acquisition process recording seismic traces with a maximum offset of ~40 km. The vibroseis data were correlated to yield 12.0-s-

long records, potentially recording reflections from interfaces as deep as 36 km (assuming an average P-wave velocity of 6 km/s).

The processing of the Larder Lake ME321-R1 seismic data was focused on appropriate binning of a crooked survey line, robust static solutions, detailed velocity analysis, minimal trace smoothing, and high-resolution imaging using a pre-stack time migration algorithm. Figure 3a shows the final migrated seismic section for ME321-R1 transects. We have also used the curvelet transform (Candès et al., 2006; Naghizadeh and Sacchi, 2010) to enhance the dip coherency of strong seismic events and the result is depicted in Figure 3c. More details on Metal Earth seismic data acquisition and processing methods can be found in Naghizadeh et al. (2019). The location of the CLLF shear zone and LNF are marked with arrows on top of the seismic section. Figure 1a shows the location and common mid-point (CMP) numbers of the seismic transect ME321-R1.

The Lithoprobe project (Hammer et al., 2010) collected several seismic transects in the Abitibi subprovince of the Superior province. Figure 1a shows the location and the CMP numbers of the Lithoprobe's KSZ12 seismic transects that is located in the vicinity of Larder Lake area and Figure 3b shows the final migrated seismic section. The KSZ12 seismic profile is oriented in north-south direction perpendicular to the dominate geological strike direction in the Abitibi subprovince. The KSZ12 seismic section was also enhanced by a dip-coherency filter applied using curvelet transform (Naghizadeh and Sacchi, 2010) and the result is shown in Figure 3d. The locations of two major shear zones in the central Abitibi, namely the CLLF and PDF, was marked on top of the seismic section.

4. Passive Seismic Survey

An active seismic reflection survey uses a controlled source of seismic energy, explosives or a vibroseis truck, and the reflected seismic energy to image the subsurface structure. On the other hand, passive seismic methods can image the subsurface by recording and analyzing the natural background seismic noise without any active seismic source in a relatively inexpensive and non-invasive way. At Larder Lake area, a passive seismic survey was carried out during spring and summer of 2019 using 40 broadband multi-component Guralp 3T seismometers at a nominal inter-station distance of 1 km. The filled black triangles in Figure 1a show the location of the seismometers which were deployed along the Larder Lake active seismic transect. The recording time was for ~40 days continuously from the 25 of May to the 4 of July 2019. During this period, 22 teleseismic events with magnitudes larger than 5 were identified and used for receiver function (RF) analysis in order to generate a 70 km deep P-S convertibility model. Also, the 40 day-long continuous ambient noise recorded by the array was used for ambient-noise surface-wave tomography (ANSWT) to produce a shear-wave velocity model to a depth of 10 km.

4.1. Ambient Noise Surface Wave Tomography (ANSWT)

The ANSWT method utilizes the correlation of the background (ambient) noise recorded at multiple seismic stations (sensors) to produce an image of subsurface structures (Campillo, 2006). Correlations of seismic ambient noise recorded at two stations can be used to reconstruct the subsurface responses as if one of the receivers was acting as a source and the other one as a receiver. In general, the ambient noise with period greater than 1s (i.e. frequencies lower than 1 Hz) are associated with meteorological sources while the noises with periods lower than 1 second is mainly due to nearby human activities such as cars and machinery. Ambient noise is mostly dominated by surface waves namely Rayleigh and Love waves (Campillo and Paul, 2003; Shapiro and Campillo,

194 2004). One of the basic characteristics of the surface waves is their dispersion meaning that the waves
195 of different periods, travel at different velocities. This means that the waves with different periods are
196 sensitive to different depths since the seismic velocities generally increase with depth as the rock
197 mass becomes more compact. In this study we use the estimated group velocity of surface waves
198 recorded between seismic stations to derive an estimate of the shear-wave velocity as a function of
199 depth along the profile.

200 First, we quality checked the raw data by computing the probabilistic power-spectral density
201 (PPSD) after segmenting the data into 10-minutes long segments (McNamara and Buland, 2004).
202 Figure 4 shows the PPSD plots for four of the Larder Lake passive seismic stations. The two grey
203 curves on the plots indicate the high- and low-noise model for viable ambient noise signals (Peterson,
204 1993). These levels are computed for the survey as a whole, so are identical on the plots for all four
205 stations. Figures 4a, 4b, and 4c show the data from stations LL6, LL36, and LL19 on which the
206 recorded ambient noise is confined to the acceptable range between the low- and high-noise levels.
207 These stations show a peak at 4 s and increasing energy below 0.1 s. However, the PPSD plot for
208 station LL10 (Figure 4d) shows a signal that does not reside in the acceptable range between the
209 grey lines and has not peak at 4 s, and has a different spread at low periods. Any stations with
210 anomalous PPSD plots similar to station LL10 were excluded from further analyses. Only 26 stations
211 were used for the ANSWT after rejecting the low-quality data.

212 The cross-correlations are computed following the standard procedure of (Bensen et al.,
213 2007). The raw data are band-passed between 0.03 and 1 Hz then cut into 30 min sections (with 50%
214 overlap) and then the data patches were correlated among all available station pairs. These
215 individual correlation functions are then stacked for the whole acquisition period to obtain the

reference correlation functions which are used for the tomography. Figures 5a and 5b show all of the horizontal-horizontal (TT) and vertical-vertical (ZZ) cross-correlations, respectively, sorted by increasing interstation distance. The Rayleigh waves show an approximate propagation velocity of 3.5 km/s on the ZZ components, recognized by the alignment of peaks with slopes steeper than the red lines that have a slope of 3 km/s. The Love waves show similar characteristics, and a comparable velocity in the TT components. Figure 5c shows a semblance plot of time-frequency analysis for picking the dispersion curve of the Rayleigh wave between stations 1 and 23. The dispersion curves were only picked from the cross-correlated records with inter-station distances more than 10 km to satisfy the condition that the analysis window should contain one wavelength of the signal. The group velocities were picked at periods 2.5, 3, 3.5, 4, 4.5, 5, and 6 seconds for corresponding 154, 155, 160, 166, 165, 165, and 166 interstation paths, respectively. The unreliable group velocity picks were discarded leading to different number of paths for each period. Figure 5d shows the group velocities picked at 3 seconds period for 155 ZZ cross-correlated interstation paths. The scale in east direction is different than the north direction in Figure 5d. The group velocity shows some lateral variations with the southern and northern portions of the array exhibiting lower velocities (lighter shade of blue) than the central portion.

Figure 5d shows a strong azimuthal dependence of the velocities with the paths oriented in the NW-SE direction being slower than the NE-SW direction. This might be due to three factors: 1) the southern and northern portions of the array are actually slower and the azimuthal dependence is merely a coincidence as these sections also trend in the same direction; 2) There is a strong azimuthal anisotropy in the region (about 7%) with a fast velocity in the NE-SW direction which seems unlikely given the orientation of the geological structures in the region which is more East-

West oriented; 3) It might be a noise-sources effect if the main noise source is located either in NW or SE of the array and therefore the paths oriented with an angle from NW-SE orientation will have correlations with a higher apparent velocity. Given the geometry of the array, it is difficult to separate between the three causes and we will assume for the rest of the paper that the observed lateral variations are purely due to true isotropic velocity structure of the crust.

Next, the estimated dispersion curves for both ZZ and TT cross-correlations are inverted in the period band [2.5 - 6] s and regularized into a regular two-dimensional (2D) grid of 0.01 degrees by 0.01 degrees cells (in north and east directions, about 1 x 1 km grid) using approach described by Mordret et al. (2013). This inversion gives an output of the dispersion curve (i.e., group/phase velocity vs. frequency) at each single cell of the map. These local dispersion curves were then inverted to obtain local 1D depth profiles of shear-wave velocity. At each location in the 2D grid, the ensemble of best local depth model is selected and used to construct the final three-dimensional (3D) shear-wave velocity model. We used a Monte-Carlo approach to invert the dispersion curves at depth because of the strong non-linearity of the problem and the absence of an accurate prior velocity model. This Monte-Carlo approach is based on a neighbourhood algorithm (Sambridge, 1999) and is described in details by Mordret et al. (2014). This algorithm has the advantage of exploring the entire model space using a Voronoi cell discretization while increasing the focus on its most promising areas as the number of iteration increases. In addition, the ensemble of all estimated models can be used to estimate the uncertainties on the model parameters.

Figure 6a shows the areal coverage the estimated shear-wave velocity model (black rectangle) projected on the lithological map of the Larder Lake area (see Figure 1 for the lithological legend). Figures 6b-6f show five depth slices of the shear-wave velocity model at 1, 3, 5, 7, and 9 km,

respectively, estimated using the simultaneous stochastic inversion of both ZZ and TT data. Parts of the model with more than ±50 m/s uncertainty for the estimated shear-wave velocity have been overlain with a semi-transparent grey tone. At the shallow depth of ~1 km, the area north of CLLF (indicated by the red line on Figure 6a) shows a high velocity anomaly (H1) while the areas to the south of the CLLF predominantly has a low-velocity anomaly (L1). The estimated uncertainty for the H1 high-velocity unit is low and therefore can be confidently associated to the mafic volcanic rocks of the Lower Blake River group. At deeper parts of the model, there is a high velocity anomaly in the north part of the model (indicated as H2 in Figure 6) starting around ~4-5 km depth and extending to 10 km depth (the bottom of the estimated model). Closer to the CLLF there is a low velocity anomaly (L2) at the depths of 7-10 km, which also has a high certainty, possibly corresponding to felsic volcanic/intrusive rocks.

4.2. Receiver Functions Analysis

Receiver function analysis is a passive imaging method for detecting the acoustic impedance discontinuities beneath a single or a network of 3-component seismic stations. It utilizes the conversion of P to S waves on a subsurface interface of seismic waves that are arriving from a distant earthquake. Receiver functions are generated by deconvolving the radial and transverse components of seismic records from the vertical components (Langston, 1979; Owens et al., 1984; Ligorría and Ammon, 1999). The deconvolution technique enhances the low-amplitude P to S converted phases and removes the source and path effects, which differ for different earthquakes, making it possible to stack or migrate the receiver functions. For the Larder Lake passive seismic project, 22 teleseismic events, with magnitudes larger than 5 and epicenteral distances between 30° and 100°, were used for receiver function analysis. Figure 7a shows the distribution of the teleseismic events used for the receiver functions analysis method. The colour of the circles indicates the number of selected receiver

functions for each event and the size of the circles is proportional to the magnitude of the events. Figure 7b depicts an example of vertical-component seismographs recorded by various stations of the array from a M6.4 earthquake in Chili, where the data have been band-pass filtered between 0.2 and 1 Hz. The blue traces were delayed due to time issues and were corrected before the deconvolution.

We used the iterative time domain deconvolution technique introduced by Ligorría and Ammon (1999) to extract the receiver functions from the raw seismograms. The main procedure involved a cosine function tapering of seismic records, band-pass filtering, deconvolving the first 60 s of the radial and transverse components of seismograms from the vertical components using a maximum of 300 iterations, and convolving the derived receiver functions (spikes) with a Gaussian filter. Figure 7c shows the estimated receiver functions for the radial components of station LL23 from various teleseismic events. The back-azimuth (b), epicentral distance (d), and magnitude (m) of each event is labelled on the right side of each receiver function. The blue-coloured traces are the receiver functions that are then stacked to generate the final receiver function (trace on the top of Figure 7c) while the grey-coloured traces were discarded as they contained anomalous amplitudes. This procedure was applied on 4 different frequency bands of the records: very low frequency 0.1-0.5 Hz (VLF), low frequency 0.2-0.8 Hz (LF), high frequency 0.5-2.0 Hz (HF), and very high frequency 0.8-3.0 Hz (VHF). Figures 7d and 7e show the stacked receiver functions on all of the available stations for VLF and HF bands, respectively. The distinct high amplitude event seen around 5 s in both VLF and HF sections corresponds to the Moho discontinuity and gives us confidence that the results are reasonable.

We used the VLF receiver function to estimate the mean Moho depth (H) and the mean crustal Vp/Vs ratio (K) beneath the array using the different moveout curves of the PS (converted P-

305 to S-wave at Moho boundary) and PpS (converted S-wave at Moho from reflected P-wave at the
306 surface) phases and assuming Vp = 6.3 km/s, determined through a grid-search approach (Zho and
307 Kanamori, 2000) . The PS phases generated at the Moho appear as a clear peak at ~5 s with the
308 expected moveout curve and the PpS phase is observed at ~16 s with an opposite moveout curve.
309 Our analysis revealed an overall estimate of H=41 km depth for the Moho and a mean Vp/Vs=1.75
310 along the Larder Lake profile. Finally, we migrated the receiver functions using the "Common
311 Conversion Point" method (Dueker and Sheehan, 1997) to reposition the depth of the interfaces that
312 generated various P to S conversions.

313 Figures 8a - 8d shows the P-S convertibility profiles for VLF, LF, HF, and VHF bands
314 projected on to the straight AB transect (depicted in Figure 1a), respectively. The Moho
315 discontinuity is clearly imaged at ~40 km in all P-S convertibility plots. Based on the identified Moho
316 depth from the seismic reflection transects and previous Moho depth studies (REF), the optimal
317 location of the Moho boundary is determined to be on the through value (negative convertibility)
318 which is immediately followed by a peak value (negative convertibility). We adopt this notion
319 (through followed by peak) as indication of shear-wave velocity increase from the top layer to the
320 layer beneath, which will be used to interpret the convertibility profiles at other parts of the profile.
321 There is also a strong south-dipping conversion, S1, that begins at Moho depth and descends into the
322 Mantle. The S1 boundary is located on a through and is followed by a strong peak in indicating the
323 penetration of a high velocity slab into the mantle. The crustal conversions will be analyzed and
324 discussed in the next section by integrating them with other geophysical data.

5. Integrated Interpretations

We begin with the integrated interpretation of two reflection seismic profiles and the regional magnetic anomaly map. The KSZ12 seismic transect is located in a close proximity (~15 km to the west) and parallel to Metal Earth's ME321-R1 seismic line. A close inspection of these 2 profiles helps to extrapolate and interpret similar seismic reflections evident on both sections. Figure 9a and 9b show the KSZ12 seismic transect overlaid by the assemblage and magnetic anomaly map to the west side of the transect. Figure 9c and 9d depict the ME321-R1 seismic transect with overlaid assemblage and magnetic anomaly map to the west of the transect, respectively. The locations of the CLLF and PDF were indicated on all four subplots in Figure 9. A collection of strong and parallel reflections indicated by G1 in Figure 9a start from depths of ~15 km and extend upward to connect with Lower Blake River volcanic units on the surface. In Figure 9b, the Lower Blake River units show parallel magnetic anomalies to the south of the PDF that extend in East-West direction. The G1 reflections strongly correlate to these parallel magnetic anomalies indicating that theses strong reflections were generated by the alternating high and lower Fe-bearing tholeiitic mafic volcanic units in Lower Blake River assemblage.

The dipping G1 reflections are terminated at the depth of ~15 km and beneath it a new set of sub-horizontal strong reflections starts. This boundary (dashed thick purple line on Figure 9b) represents the base of the upper crust in the Abitibi greenstone belt. The synformal G2 reflections (green dashed line) correspond to the Upper Blake River volcanic group. The Moho boundary is located at approximate depth of 40 km where the seismic reflections stop (red dashed line). The dimmed reflection zone of M1 cuts through lower- and middle-crustal material and reaches to the upper-crust where the reflections become even dimmer. This dimmed reflection zone between G2 and G3 likely has near vertical layer boundaries which the seismic reflection method cannot not properly

image. The G3 antiform reflections to the south of the dimmed upper-crust zone likely correspond to a volcanic unit. The CLLF shear zone under the KSZ12 transect (Figure 9a) terminates the shallow reflection to the south and G3 reflections to the north and can be extrapolated down to the the boundary of the upper- and middle-crust, where there is a small upwards displacement of the southern block.

About 10 km to the east and beneath the ME321-R1 transect (Figure 9c), the CLLF truncates the G4 upper-crust reflections as well as the sub-horizontal middle- and lower-crust reflections and extends towards the Moho discontinuity. The upper-crust under the ME321-R1 transect shows two sets of strong north-dipping reflections, G4 and G5, separated by a fault which can be traced to the surface location of the Mulvan Lake Fault (MLF). Also, the G5 reflections are terminated to the north by a vertically dipping fault which is interpreted to be Misma-Mist Lakes Fault (MMF). The boundary between upper- and middle-crust (thick purple dashed line) is interpreted here to be in a deeper position under the ME321-R1 transect compared to the KSZ12 transect. At the northern limits of the ME321-R1 transect, the upper-crust starts to show sub-horizontal to gently-south-dipping reflections that could be related to the Lower Blake River Volcanic assemblage similar to G1 reflections under the KSZ12 transect. The dimmed reflection zone M2 below the ME321-R1 transect, is similar to the M1 dimmed zone under the KSZ12 transect. Both M1 and M2 dimmed reflection zones begin beneath the Upper Blake River at the lower crust depths, however, they migrate towards the south in the upper-crust closer to the CLLF shear zone. We interpret these dimmed reflection zones to be pathways for the intrusion from the mantle. Figure 9d shows the magnetic response of some of these intrusive bodies (indicated by 4 white ellipses), the northern one being in the southern parts of the Blake River group. In the northern parts of the Blake River group the magnetic

anomalies are mostly parallel and not disrupted by intrusive bodies. At the south part of ME321-R1 transect, the Lincoln-Nippising Fault (LNF) cross-cuts through a series of strong reflections in the upper-crust and extends deeper into the middle-crust. The AG23 seismic transect (Figure 3a), which extends further to the south compared with ME321-R1 transect, shows that the LNF extends deeper into the lower crust almost vertically and parallel to the CLLF shear zone.

Figure 10a shows colour overlay of the shear-wave velocity estimated using ANSWT on the ME321-R1 reflection seismic section. Figure 10b shows the same plot as Figure 10a after dimming parts of the model that have greater than ± 50 m/s uncertainty in the estimated shear-wave velocity. A strong seismic reflection separates the H1 high-velocity and L2 low-velocity anomalies. This velocity contrast and resulting strong reflection most likely was caused by a contact between a felsic volcanic/intrusive unit at the bottom and a mafic volcanic/intrusive unit at the top. The H1 anomaly is interpreted to dip toward north and at the bottom of the model the H1 anomaly is truncated by the less-certain L3 low-velocity anomaly. This interruption coincides with the interpreted position of the MMF on the seismic section in Figure 9. The L3 low-velocity anomaly which is separated by MLF (see Figure 9c) from the L2 low-velocity anomaly is interpreted to have a similar lithological compositions as the L2 anomaly. The H2 high-velocity anomaly becomes stronger and deeper toward the north of the model. The low-velocity zone at surface gets relatively thick and shows less uncertainty at L1. Below the L1 anomaly, the H3 high-velocity anomaly extends to the depth of 10 km, the bottom of the model. The less-certain H3 anomaly seems to have a slight increase in velocity around a depth of 6 km which also correlates with a series of strong seismic reflections. There is a narrow less-certain low-velocity zone between the H3 and H1 anomalies which coincides with the location of the CLLF interpreted from the seismic section. The H3 high-velocity

anomaly is truncated to the south by the L4 low-velocity anomaly, which is apparent as a low-certainty anomaly between 6-10 km depth. Overall, there are good correlations between the reflections in the seismic profile and the vertical structures that terminate these reflectors and the boundaries of the velocity anomalies derived from the ANSWT method.

Figure 11 combines all four frequency bands in Figure 8 into a single P-S convertibility profile after normalizing and summing all frequency bands. The ME321-R1 seismic transect is also shown in grey tones in the background of the P-S convertibility map in Figure 11. The most distinct and obvious P-S conversion happens at the Moho boundary around a depths of ~40 km (labelled dashed line). Below the Moho, in the the north part of the transect section there is a strong south-dipping anomaly (S1), which appears to merge with the Moho at the northern limits of the transect beneath the M2 dimmed reflection anomaly marked in Figure 9c. The S1 anomaly most likely is an oceanic crust slab that has sunk into the mantle, but could also be a layer at the base of the crust that has delaminated and sunk. At shallower depths the P-S convertibility profile and ME321-R1 reflectivity profile show matching features. The C2 and C4 low-amplitude zones of P-S conversion are terminated to the south by the CLLF, with high-amplitude features appearing at few location to the south. The C2 anomaly occurs at the same position as the L2 low-velocity anomaly in Figure 10b right beneath the strong north-dipping seismic reflections. The location and size of the C1 anomaly matches with a high correlation to the H2 high-velocity anomaly observed in Figure 10b. The slightly north-dipping C3 anomaly sits beneath strong seismic reflections evident in the ME321-R1 section, which provides strong evidence for the bottom of the upper-crust being composed of greenstones. The large C4 anomaly is coincident with a zone where sub-horizontal middle-crust reflectors are observed in the active seismic profile.

Figures 12a, 12b, and 12c depict the top 10 km of the crust from the ME321-R1 seismic transect, S-wave velocity model estimated using the ANSWT method, and P-S convertibility profile at VHF estimated using the receiver function analysis, respectively. The B1 feature coincides with the bottom of a zone of strong reflections (Figure 12a), and also marks the bottom of a low shear-wave velocity zone (Figure 12b and also L1 in Figure 10b), and matches with a through followed by a peak convertibility (an indication of a boundary between a top low velocity layer and bottom high velocity layer) in the P-S convertibility profile. The deeper B2 boundary is located on top of a package of strong north-dipping seismic reflections (Figure 12a). On the shear-wave velocity profile derived using the ANSWT method, the B2 line marks a transition from a top high velocity to bottom low velocity layer that also dips towards the north. Interestingly, the B2 curve follows a north dipping positive followed by negative convertibility value to the south (implying transition from a high to low velocity layer). The B3 line demarcates a set of horizontal seismic reflections at ~5 km depth (Figure 12a), a transition from a low to high velocity (Figure 12b), and a negative value below the positive convertibility value (Figure 12c) that is an indication of transition from a low to high velocity layer. These three features (B1, B2, and B3) show a good correlation with high confidence between the shear-wave velocity and P-S convertibility profiles estimated from passive seismic data and the active seismic transect. We have also demarcated 3 more features with grey colours (P1, P2, and P3) that show good correlations in all three depicted profiles, however, these features had larger uncertainty values in the estimated shear-wave velocity profile using the ANSWT method. Nevertheless, the good correlation between these features in three different geophysical profiles increases the confidence in the estimated shear-velocities at these locations.

Figure 13 shows a juxtaposition of the ME321-R1 and KSZ12 seismic transects and the deeper part of the P-S convertibility profile along the south-north direction. The S1 slab coincides with a south dipping reflectivity response on the KSZ12 seismic section and its continued plunge into the mantle is clearly imaged on the P-S convertibility profile. The S1 slab penetration into the mantle coincides with a dim reflection zone (M2) in the lower crust which also resulted in an upward bending of seismic reflections, R4 dashed line, at the Moho boundary. This upward push continues until the reflections reach the boundary of the lower and middle crust (R3 dashed line), which itself bends downwards. The base of the greenstone layers (R1 and R2 dashed lines) seems to be located deeper beneath the ME321-R1 transect compared to the KSZ12 transect. In the upper crust the upper and lower Blake River assemblage boundary (G2 dashed line) shows a similar depth in both ME321-R1 and KSZ12 seismic sections.

6. Discussions

The integrated interpretation of the geophysical transects obtained from active and passive seismic surveys offers new evidence for the structural evolution of the central Abitibi. The S1 slab observed in the KSZ12 seismic and P-S convertibility transects has a relatively short horizontal and vertical extensions to be caused by subduction or horizontal plate motions. We hypothesis three possible explanations for the formation of S1 slab. 1) It is likely that the S1 slab is caused by the delimination and sinking of the lower crust into the mantle and the middle crust dimmed reflection zones, M1 and M2, were caused by the intrusions from the partial melting of the slab. This interpretation is compatible with the finding of a recent study that portrates a continental-rift setting, driven by plume magmatism in the central Abitibi prior (Mole et al., 2021). 2) It could also represent a deeper segment of the PDF that was preserved below the Moho. The mildly south-

dipping PDF was interpreted to be a listeric segment of a deeper fault in the Matheson and Timmins areas (Haugaard et al., 2021). 3) It is also possible that the S1 slab is a post-Archean feature and was caused by a younger mantle intrusion and readjustment of the mantle and crustal material.

The ANSWT and receiver function analysis methods have complementary depth resolution when used for imaging the subsurface structures. The ANSWT method provides an estimate of the shear-wave velocity for the top 10 km of the subsurface. Also, the stochastic inversion approach adopted for inverting the shear-wave velocities from group velocities produces uncertainty values for the estimated velocities. The receiver function analysis, on the other hand, generates the P-S convertibility profile to a maximum depth of 70 km. While the P-S convertibility profile is assumed to be more reliable at larger depths, we found a good correlation between the P-S convertibility profile, the ANSWT shear-wave velocity, and reflection seismic transect at shallower depths (less than 10 km).

There are inherent ambiguities and uncertainties in the estimated shear-wave velocities using the ANSWT mainly due to the deployment of seismometers on a linear array rather than an areal distribution. An areal distribution of seismometers can resolve the ambiguities that could be caused by strong azimuthal anisotropy or preferential ambient noise source locations. However, in this study, the strong correlation between the reflection seismic and passive seismic transects indicates that the 1D assumption used for passive seismic processing was appropriate. Increasing the recording time for the passive seismic array can also lead to a higher-resolution estimation of surface-wave group velocities and the receiver functions.

7. Conclusions

We have acquired and processed active and passive seismic surveys along an approximately 40 km long transect in the Larder Lake area, Ontario, Canada. The passive seismic data was processed using the ANSWT and receiver function analysis methods to obtain the shear-wave velocity and P-S convertibility profiles, respectively. The migrated reflection seismic sections were enhanced using the curvelet transform for optimal dip coherency results. The termination of upper-crust dipping seismic reflection and the beginning of the middle-crust subhorizontal reflections in the ME321-R1 and KSZ12 seismic transects suggest that the base of greenstone belt is located at a depth of approximately 12 to 15 km. The receiver function analysis identified the Moho discontinuity at ~40 km as well as the presence of a south dipping slab penetrating into the mantle under the ME321-R1 transect. The ANSWT method imaged a low shear-wave velocity zone (depths of 0-2 km) to the south of the CLLF and a high shear-wave velocity zone to the north of the ME321-R1 transect (depths of 4-10 km). To the north of the CLLF, a strong north-dipping seismic reflection (at 6 km depth) was caused by a high-velocity layer (likely a mafic intrusive/volcanic unit) at the top and a low-velocity layer (likely a felsic intrusive/volcanic unit) at the bottom. The P-S convertibility (estimated using receiver function analysis) and the shear-wave velocity (estimated using the ANSWT method) profiles show a good correlation at the shallower depths (0-10 km). Both seismic reflection and P-S convertibility profiles imaged a south-dipping slab penetrating from the lower-crust into the mantle beneath the Larder Lake transect which is interpreted to be either caused by the delamination of lower crust or a possible deeper extension of the PDF. The integrated interpretation of the geophysical models (reflectivity, shear-wave velocity, and P-S convertibility) revealed a detailed image of the subsurface lithological boundaries on the top 10 km with high confidence and good correlation values. Our results indicate that the properly designed passive seismic surveys are viable

alternatives to active seismic surveys with the added benefit of cheaper acquisition costs and less environmental impacts.

8. Data Availability Statement

The reflection seismic sections, shear-wave velocity volume, and P-S convertibility sections can be obtained from the Metal Earth Data Repository (https://merc.laurentian.ca/research/metal-earth/public-data) and Open Science Framework (https://osf.io/). We are currently in the process of uploading these datasets into the above-mentioned data repositories and upon the final acceptance of the article we will provide the exact download link for the data.

9. Acknowledgements

The authors thank Canada First Research Excellence Fund for financial support to the multidisciplinary mineral exploration research project Metal Earth. The QGIS and OpendTect software were used for data visualization and we thank their developers.

10. References

Ammon, C. J., 1991, The isolation of receiver effects from teleseismic P waveforms: Bulletin - Seismological Society of America, **81**, 2504–2510.

Ayer, J., P. C. Thurston, R. Bateman, B. Dubé, H. L. Gibson, M. A. Hamilton, B. Hathway, S. M. Hocker, M. Houlé, G. J. Hudak, V. Ispolatov, B. Lafrance, C. M. Lesher, P. J. MacDonald, A. S. Péloquin, S. J. Piercey, L. E. Reed, and P. H. Thompson, 2005, Overview of Results from the Greenstone Architecture Project: Discover Abitibi Initiative: Ontario Geological Survey.

Ayer, J., Y. Amelin, F. Corfu, S. Kamo, J. Ketchum, K. Kwok, and N. Trowell, 2002, Evolution of the southern Abitibi greenstone belt based on U-Pb geochronology: Autochthonous

volcanic construction followed by plutonism, regional deformation and sedimentation: Precambrian Research, **115**, 63–95.

Bédard, J. H., 2018, Stagnant lids and mantle overturns: Implications for Archaean tectonics, magmagenesis, crustal growth, mantle evolution, and the start of plate tectonics: Geoscience Frontiers, **9**, 19–49.

Bédard, J. H., and L. B. Harris, 2014, Neoarchean disaggregation and reassembly of the Superior craton: Geology, **42**, 951–954.

Bensen, G. D., M. H. Ritzwoller, M. P. Barmin, A. L. Levshin, F. Lin, M. P. Moschetti, N. M. Shapiro, and Y. Yang, 2007, Processing seismic ambient noise data to obtain reliable broad-band surface wave dispersion measurements: Geophysical Journal International, **169**, 1239–1260.

Calvert, A. J., E. W. Sawyer, W. J. Davis, and J. N. Ludden, 1995, Archaean subduction inferred from seismic images of a mantle suture in the Superior Province: Nature, **375**, 670–674.

Campillo, M., 2006, Phase and correlation in "random" seismic fields and the reconstruction of the green function: Pure and Applied Geophysics, **163**, 475–502.

Campillo, M., and A. Paul, 2003, Long range correlations in the diffuse seismic coda: Science, **299**, 547–549.

Candès, E., L. Demanet, D. Donoho, and L. Ying, 2006, Fast discrete curvelet transforms: Multiscale Modeling and Simulation, **5**, 861–899.

Clowes, R. M., F. A. Cook, A. G. Green, C. E. Keen, J. N. Ludden, J. A. Percival, G. M. Quinlan, and G. F. West, 1992, Lithoprobe: new perspectives on crustal evolution: Canadian Journal of Earth Sciences, **29**, 1813–1864.

Corfu, F., S. L. Jackson, and R. H. Sutcliffe, 1991, U-Pb ages and tectonic significance of late Archean alkalic magmatism and nonmarine sedimentation: Timiskaming Group, southern Abitibi Belt, Ontario: Canadian Journal of Earth Sciences, **28**, 489–503.

Davis, W. J., S. Lacroix, C. Gariépy, and N. Machado, 2000, Geochronology and radiogenic isotope geochemistry of plutonic rocks from the central Abitibi subprovince: Significance to the internal subdivision and plutono-tectonic evolution of the Abitibi belt: Canadian Journal of Earth Sciences, **37**, 117–133.

Dueker, K. G., and A. F. Sheehan, 1997, Mantle discontinuity structure from midpoint stacks of converted P to S waves across the Yellowstone hotspot track: Journal of Geophysical Research: Solid Earth, **102**, 8313–8327.

Hammer, P. T. C., R. M. Clowes, F. A. Cook, A. J. van der Velden, and K. Vasudevan, 2010, The Lithoprobe trans-continental lithospheric cross sections: Imaging the internal structure of the North American continent: Canadian Journal of Earth Sciences, **47**, 821–857.

Haugaard, R., F. Della Justina, E. Roots, S. Cheraghi, R. Vayavur, G. Hill, D. Snyder, J. Ayer, M. Naghizadeh, and R. Smith, 2021, Crustal-Scale Geology and Fault Geometry Along the Gold-Endowed Matheson Transect of the Abitibi Greenstone Belt: Economic Geology.

Hyde, R. S., 1980, Sedimentary facies in the Archean Timiskaming Group and their tectonic implications, abitibi greenstone belt, Northeastern Ontario, Canada: Precambrian Research, **12**, 161–195.

Jackson, S. L., and A. R. Cruden, 1995, Formation of the Abitibi greenstone belt by arc-trench migration: Geology, **23**, 471–474.

Jackson, S. L., A. R. Cruden, D. White, and B. Milkereit, 1995, A seismic-reflection-based regional cross section of the southern Abitibi greenstone belt: Canadian Journal of Earth Sciences, **32**, 135–148.

Van Kranendonk, M. J., W. J. Collins, A. Hickman, and M. J. Pawley, 2004, Critical tests of vertical vs. horizontal tectonic models for the Archaean East Pilbara Granite-Greenstone Terrane, Pilbara Craton, Western Australia: Precambrian Research, **131**, 173–211.

Langston, C. A., 1979, Structure under Mount Rainier, Washington, inferred from teleseismic body waves.: Journal of Geophysical Research, **84**, 4749–4762.

Ligorría, J. P., and C. J. Ammon, 1999, Iterative deconvolution and receiver-function estimation: Bulletin of the Seismological Society of America, **89**, 1395–1400.

McNamara, D. E., and R. P. Buland, 2004, Ambiente noise levels in the continental United States: Bulletin of the Seismological Society of America, **94**, 1517–1527.

Mole, D. R., P. C. Thurston, J. H. Marsh, R. A. Stern, J. A. Ayer, L. A. J. Martin, and Y. J. Lu, 2021, The formation of Neoarchean continental crust in the south-east Superior Craton by two distinct geodynamic processes: Precambrian Research, **356**.

Montsion, R., P. Thurston, and J. Ayer, 2018, 1:2000000 Scale Geological Compilation of the Superior Craton: Mineral Exploration Research Centre.

584 Mordret, A., M. Landés, N. M. Shapiro, S. C. Singh, and P. Roux, 2014, Ambient noise surface
585 wave tomography to determine the shallow shear velocity structure at Valhall: Depth
586 inversion with a Neighbourhood Algorithm: Geophysical Journal International, **198**, 1514–
587 1525.

588 Mordret, A., M. Landés, N. M. Shapiro, S. C. Singh, P. Roux, and O. I. Barkved, 2013, Near-
589 surface study at the valhall oil field from ambient noise surface wave tomography:
590 Geophysical Journal International, **193**, 1627–1643.

591 Mueller, W., J. A. Donaldson, and P. Doucet, 1994, Volcanic and tectono-plutonic influences on
592 sedimentation in the Archaean Kirkland Basin, Abitibi greenstone belt, Canada:
593 Precambrian Research, **68**, 201–230.

594 Naghizadeh, M., and M. D. M. D. Sacchi, 2010, Beyond alias hierarchical scale curvelet
595 interpolation of regularly and irregularly sampled seismic data: Geophysics, **75**, WB189–
596 WB202.

597 Naghizadeh, M., D. Snyder, S. Cheraghi, S. Foster, S. Cilensek, E. Floreani, and J. Mackie,
598 2019, Acquisition and processing of wider bandwidth seismic data in crystalline crust:
599 Progress with the Metal Earth project: Minerals, **9**, 145.

600 Owens, T. J., G. Zandt, and S. R. Taylor, 1984, Seismic Evidence for an Ancient Rift Beneath
601 the Cumberland Plateau, Tennessee: a Detailed Analysis of Broadband Teleseismic P
602 Waveforms.: Journal of Geophysical Research, **89**, 7783–7795.

603 Percival, J. A., M. Sanborn-Barrie, T. Skulski, G. M. Stott, H. Helmstaedt, and D. J. White,
604 2006, Tectonic evolution of the western Superior Province from NATMAP and Lithoprobe
605 studies: Canadian Journal of Earth Sciences, **43**, 1085–1117.

606 Peterson, J., 1993, Observations and modeling of seismic background noise: U.S. Department of
607 Interior Geological Survey, **Open-File**.

608 Powell, W. G., D. M. Carmichael, and C. J. Hodgson, 1995, Conditions and timing of
609 metamorphism in the southern Abitibi Greenstone Belt, Quebec: Canadian Journal of
610 Earth Sciences, **32**, 787–805.

611 Sambridge, M., 1999, Geophysical inversion with a neighbourhood algorithm - I. Searching a
612 parameter space: Geophysical Journal International, **138**, 479–494.

613 Shapiro, N. M., and M. Campillo, 2004, Emergence of broadband Rayleigh waves from
614 correlations of the ambient seismic noise: Geophysical Research Letters, **31**, 8–11.

615 Thurston, P. C., J. A. Ayer, J. Goutier, and M. A. Hamilton, 2008, Depositional gaps in abitibi
616 greenstone belt stratigraphy: A key to exploration for syngenetic mineralization: Economic
617 Geology, **103**, 1097–1134.

618 Van-Hunen, J., and J.-F. Moyen, 2012, Archean Subduction: Fact or Fiction? The Annual
619 Review of Earth and Planetary Sciences Is Online at Earth.Annualreviews.Org, **40**, 195–
620 219.

621 White, D. J., G. Musacchio, H. H. Helmstaedt, R. M. Harrap, P. C. Thurston, A. der Velden, K.
622 Hall, A. Van der Velden, and K. Hall, 2003, Images of a lower-crustal oceanic slab: Direct
623 evidence for tectonic accretion in the Archean western Superior province: Geology, **31**, 997–
624 1000.

625 Zho, L., and H. Kanamori, 2000, Moho depth variation in southern California from teleseismic
626 receiver functions: Journal of Geophysical Research, **105**, 2969–2980.

627

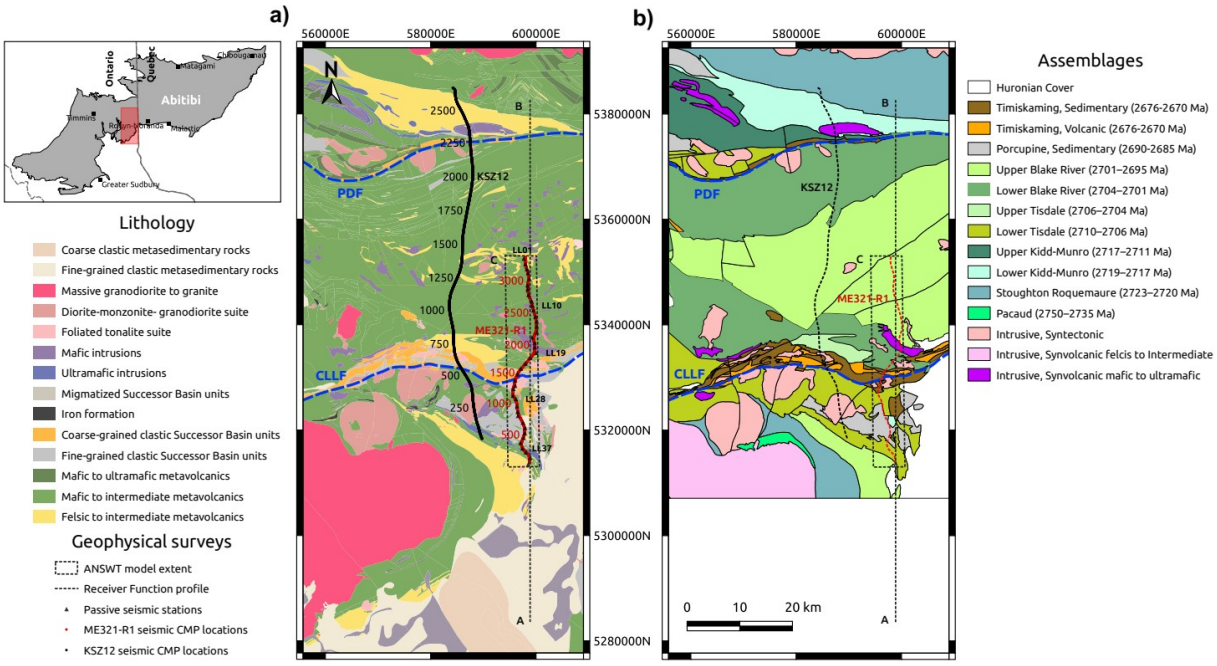

Figure 1: a) The lithological map of Larder Lake area. The final processed Larder Lake seismic line (ME321-R1) was shown by red circles and the red colour numerals show the CMP locations. The location of passive seismic stations are shown using filled black triangles that closely follow the ME321 seismic line. The black points show the Lithoprobe's KSZ12 profile and black numerals show its CMP locations. The dashed line AB shows the traverse imaged by the receiver function method and the dashed rectangle C shows the area that was imaged using the ANSWT method. b) The corresponding assemblage map of the lithological units shown in (a). Spatial coordinates are in the UTM NAD83 Zone N17 coordinate system.

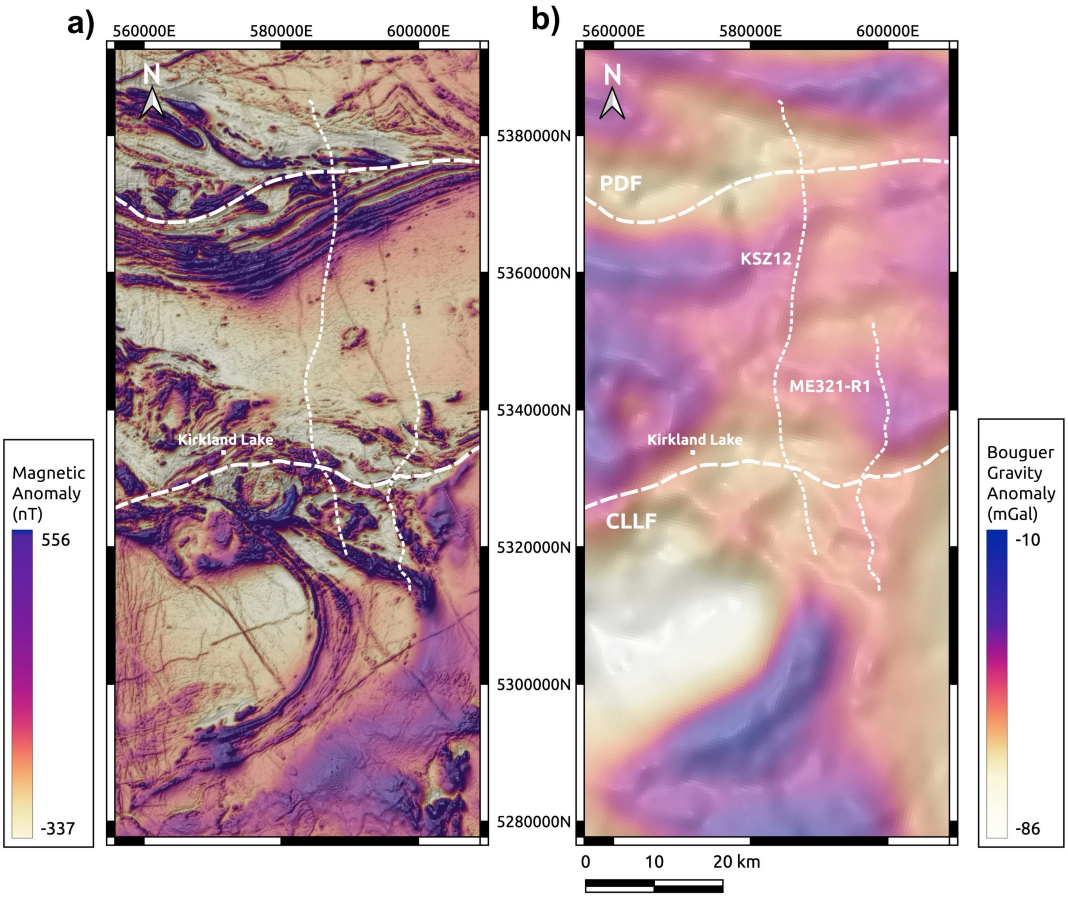

Figure 2: a) The magnetic anomaly and b) Bougeur gravity anomaly maps of the Larder Lake area. The reflection seismic transects were shown by dashed white lines.

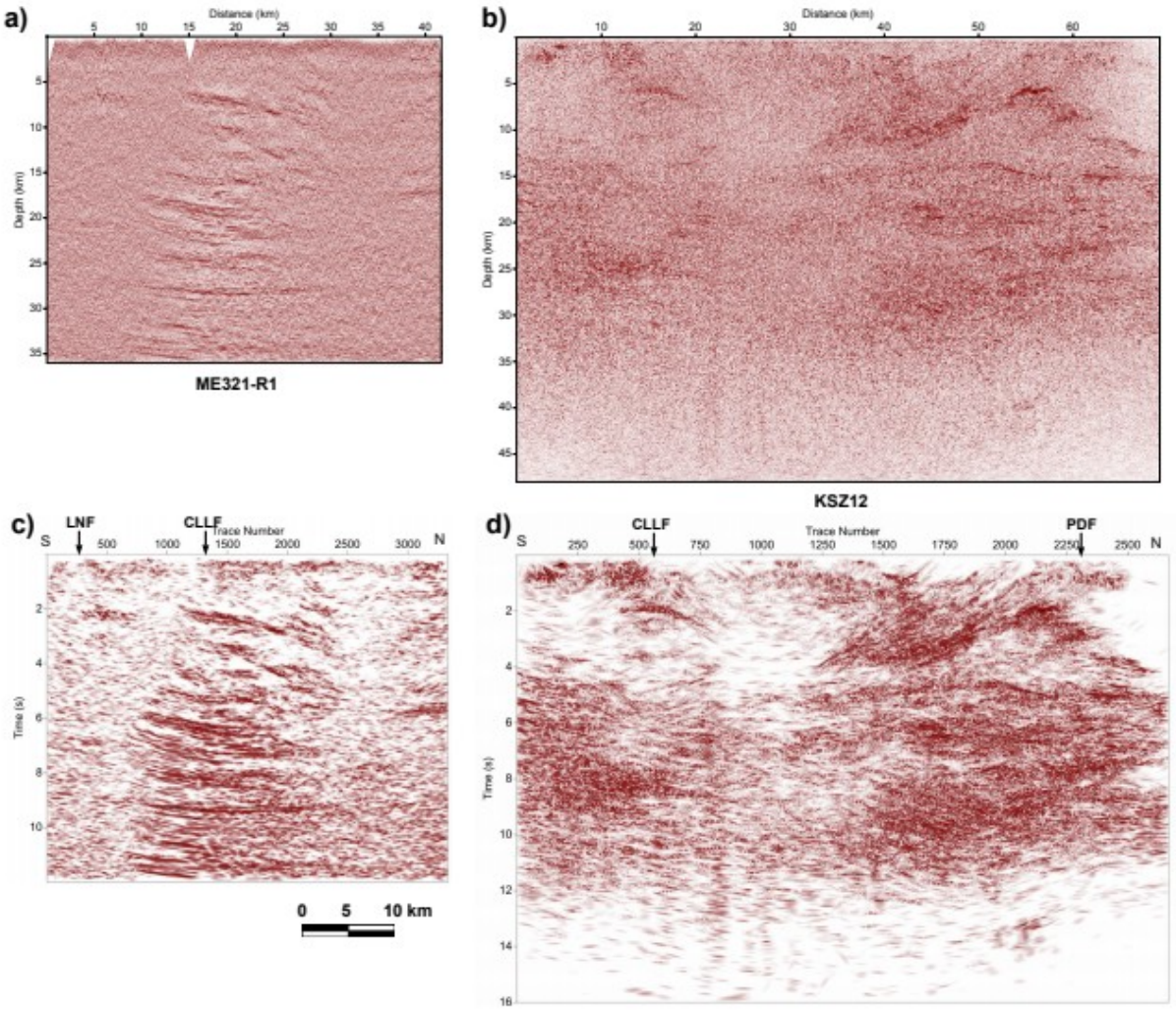

Figure 3: a) The Metal Earth ME321-R1 seismic transect. b) The Lithoprobe KSZ12 seismic transect. c) and d) are the dip-coherency enhancements of a and b using the curvelet transform, respectively. The plots a and b are depicted with distance and depth axes, while c and d are plotted with trace number and time axes. Time to depth conversion of seismic sections was done based on the assumption of constant velocity of 6 km/s. The locations of major geological faults (CLLF, PDF, and LNF) are marked in c and d.

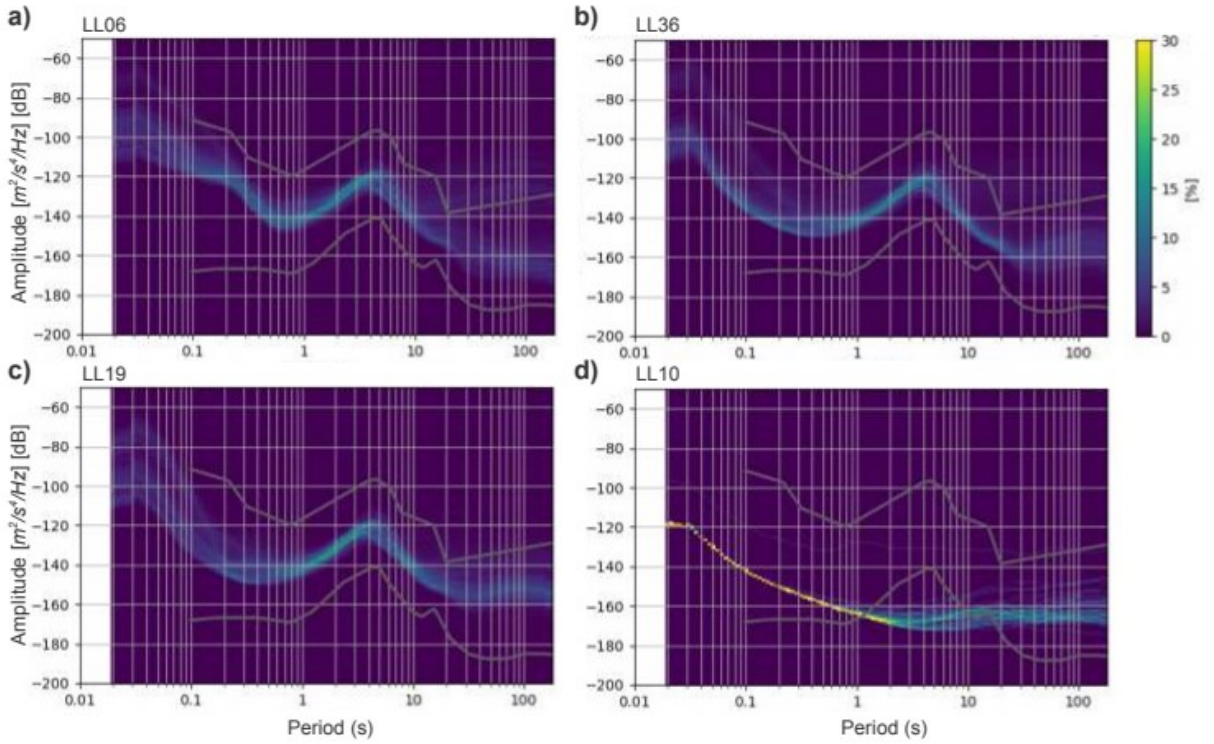

Figure 4: a)- d) show the probabilistic power-spectral density (PPSD) plots for the stations LL06, LL36, LL19, and LL10, respectively. The gray curves on the plots show the low and high limits for viable ambient noise signals. The PPSD plot of station LL10 shows signal outside the acceptable limit and therefore it was excluded for inter-station group velocity estimations.

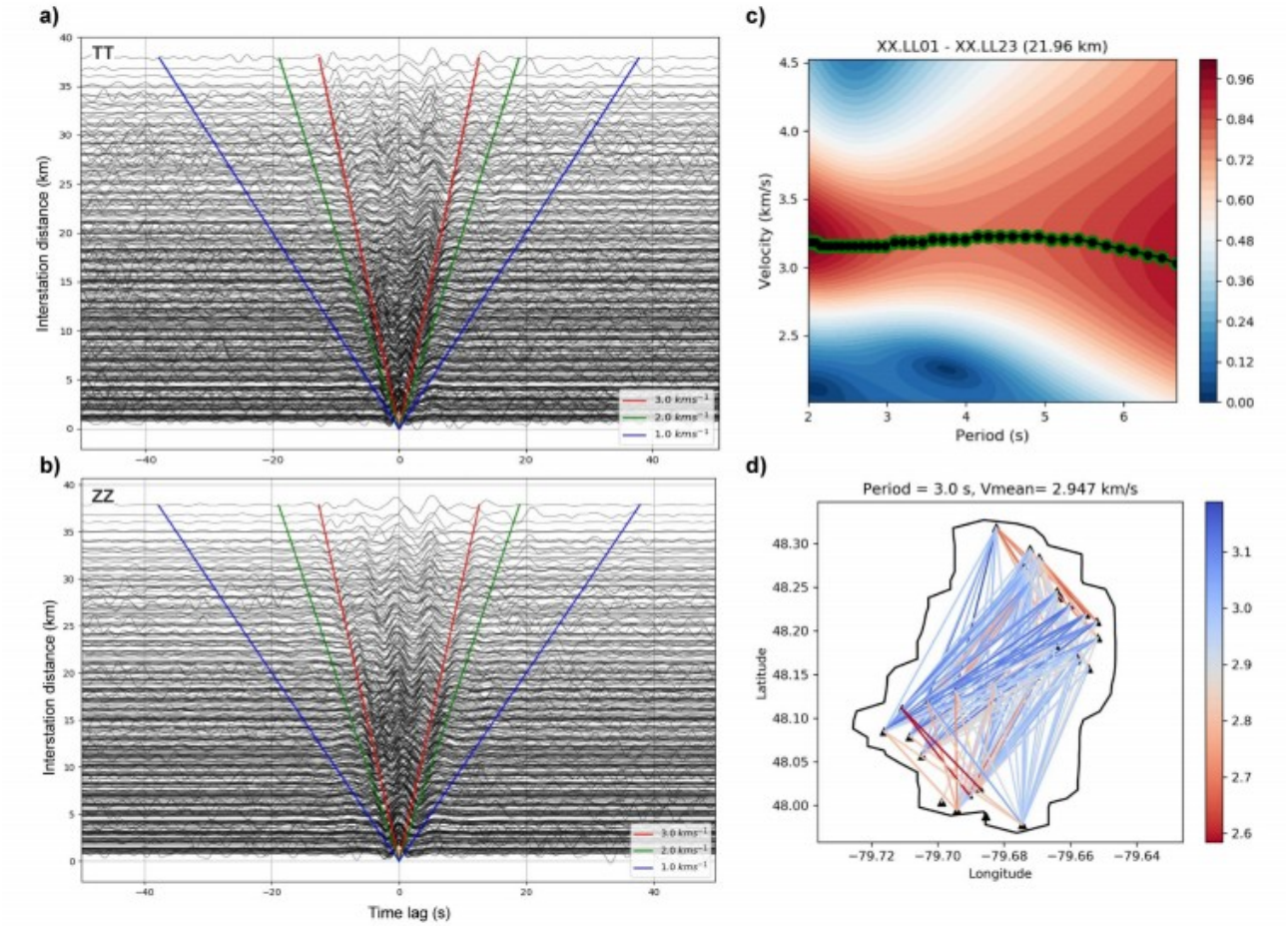

Figure 5: a) and b) show all of the horizontal-horizontal (TT) and vertical-vertical (ZZ) cross-correlations of ambient noise, respectively, sorted by increasing interstation distances. c) Surface-wave dispersion curve estimated between the stations LL01 and LL23. d) The estimated group velocity values for all possible pairs of stations with a minimum interstation distance of 10 km at 3 sec period (notice that the longitude axis is stretched in this plot).

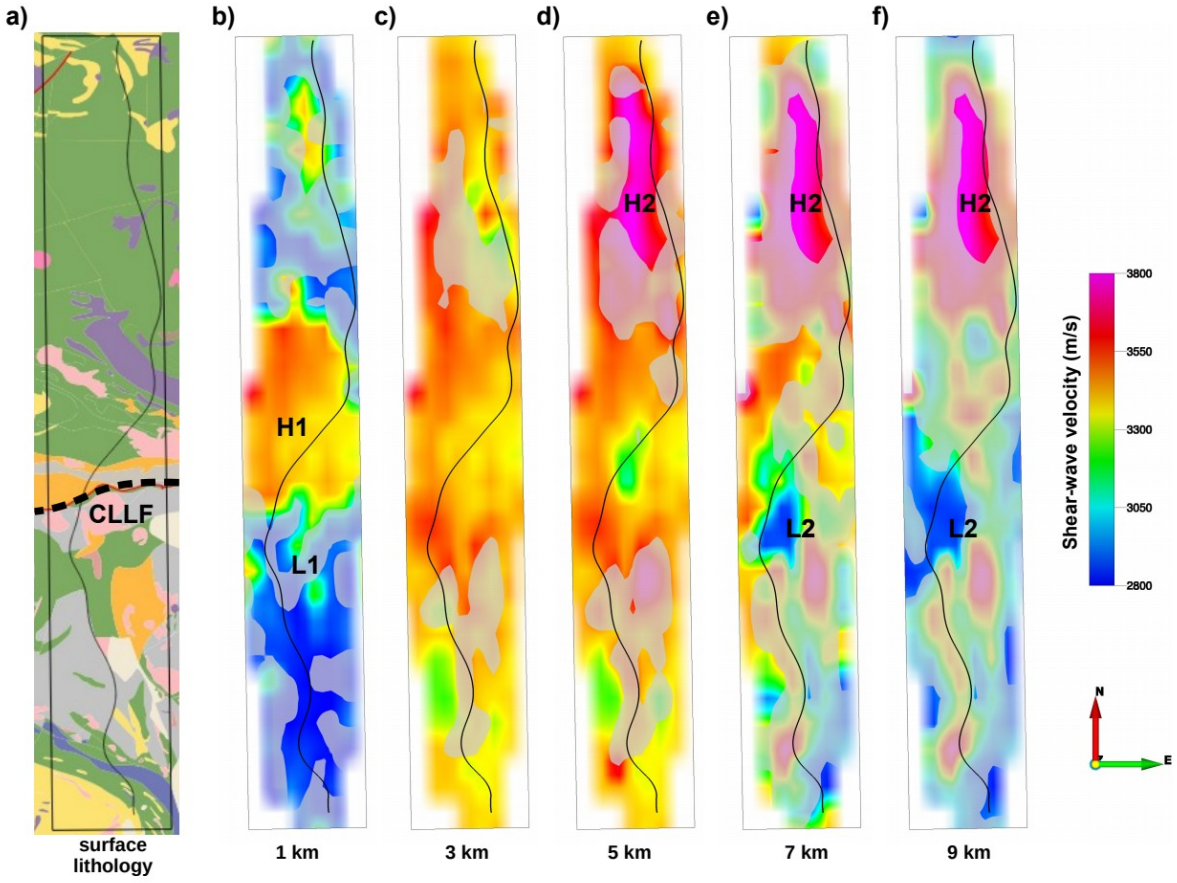

Figure 6: a) The lithological map of the larder lake area in the vicinity of the passive seismic array. The curved black line shows the location of ME321-R1 seismic transect. The region marked by the black rectangle is the same as the dashed rectangle C in Figure 1a. b) to f) show the depth slices of the estimated shear-wave velocity using the ANSWT method at depths of 1, 3, 5, 7, and 9 km, respectively. The dimmed regions of the model have more than ±50 m/s uncertainty for the estimated shear-wave velocities.

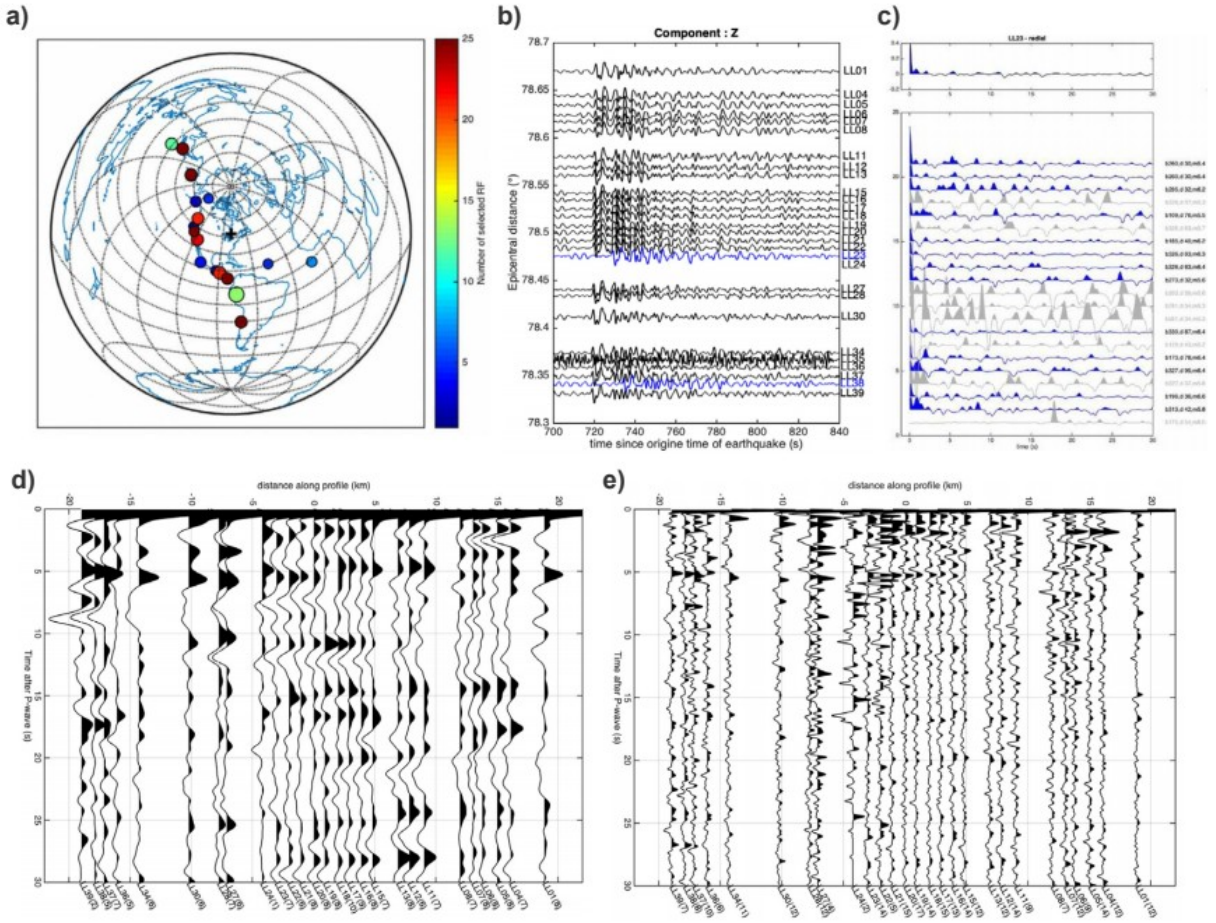

Figure 7: a) The location of earthquakes used for receiver function analysis (the size of circles represents the magnitude of the earthquakes and the colour represents the number of selected receiver functions). b) The vertical component of a seismographs recorded by Larder Lake array from an earthquake in Chile. The blue-coloured traces were time-shifted due to timing issues and were corrected before further analyses. c) The estimated receiver functions for the radial components of station LL23 from different earthquakes (bottom) and final stacked receiver functions (top). The grey-coloured receiver functions were discarded due to the high level of noise. d) and e) The final estimated receiver functions for Larder Lake passive seismic stations for the VLF (0.1-0.5 Hz) and HF (0.5-2.0 Hz) ranges, respectively.

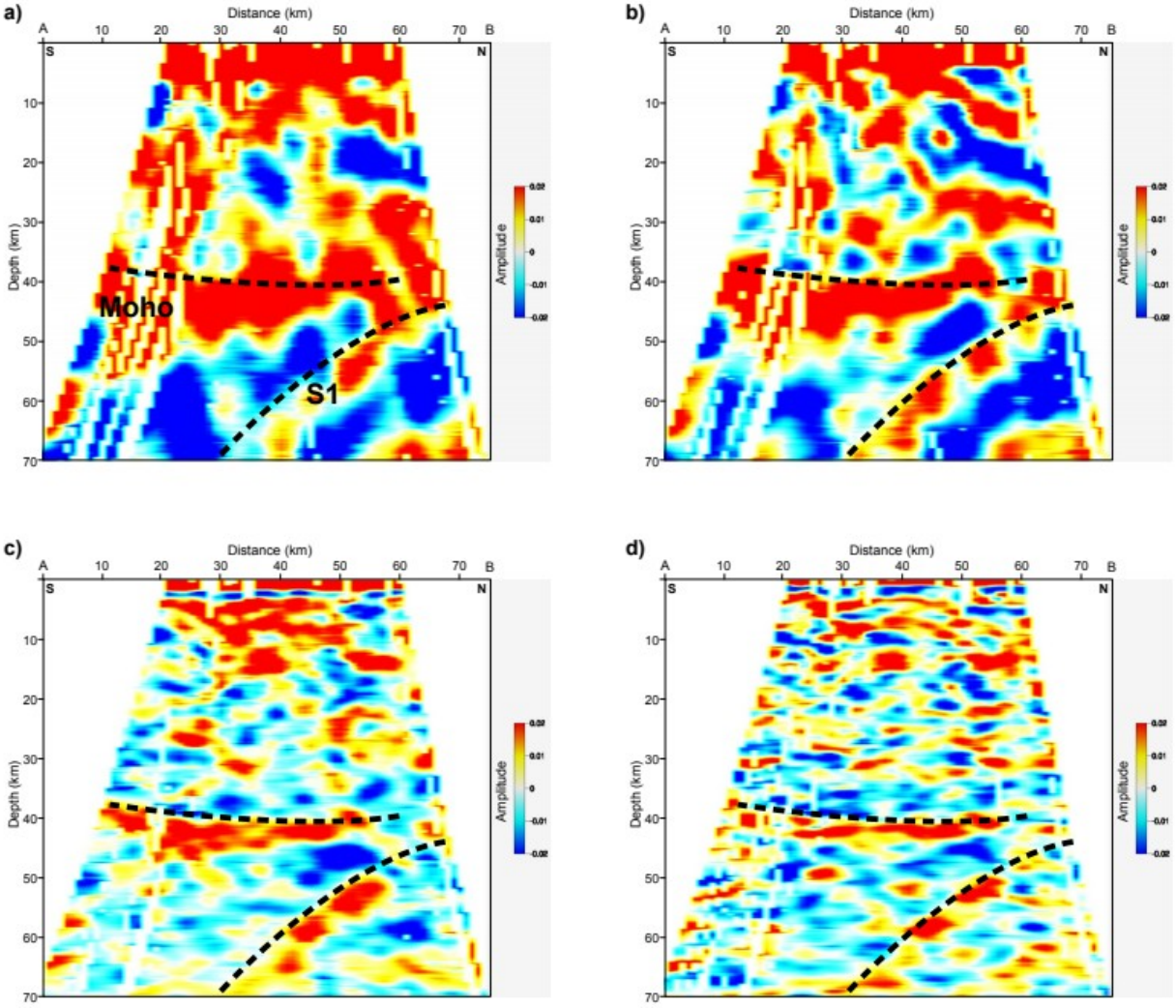

Figure 8: a) -d) are the P-S convertibility profiles estimated using the receiver function analysis for the VLF (0.1-0.5 Hz), LF (0.2-0.8 Hz), HF (0.5-2.0 Hz), and VHF (0.8-3.0 Hz) bands, respectively. The location of the traverse AB is shown in Figure 1. The convertibility is a similar concept to the reflectivity, however, it is an indication of elastic rock property variations in the subsurface that results in P- to S-wave conversions. The Moho discontinuity at depth of ~40 km and a south-dipping slab (S1) were imaged in all four frequency bands.

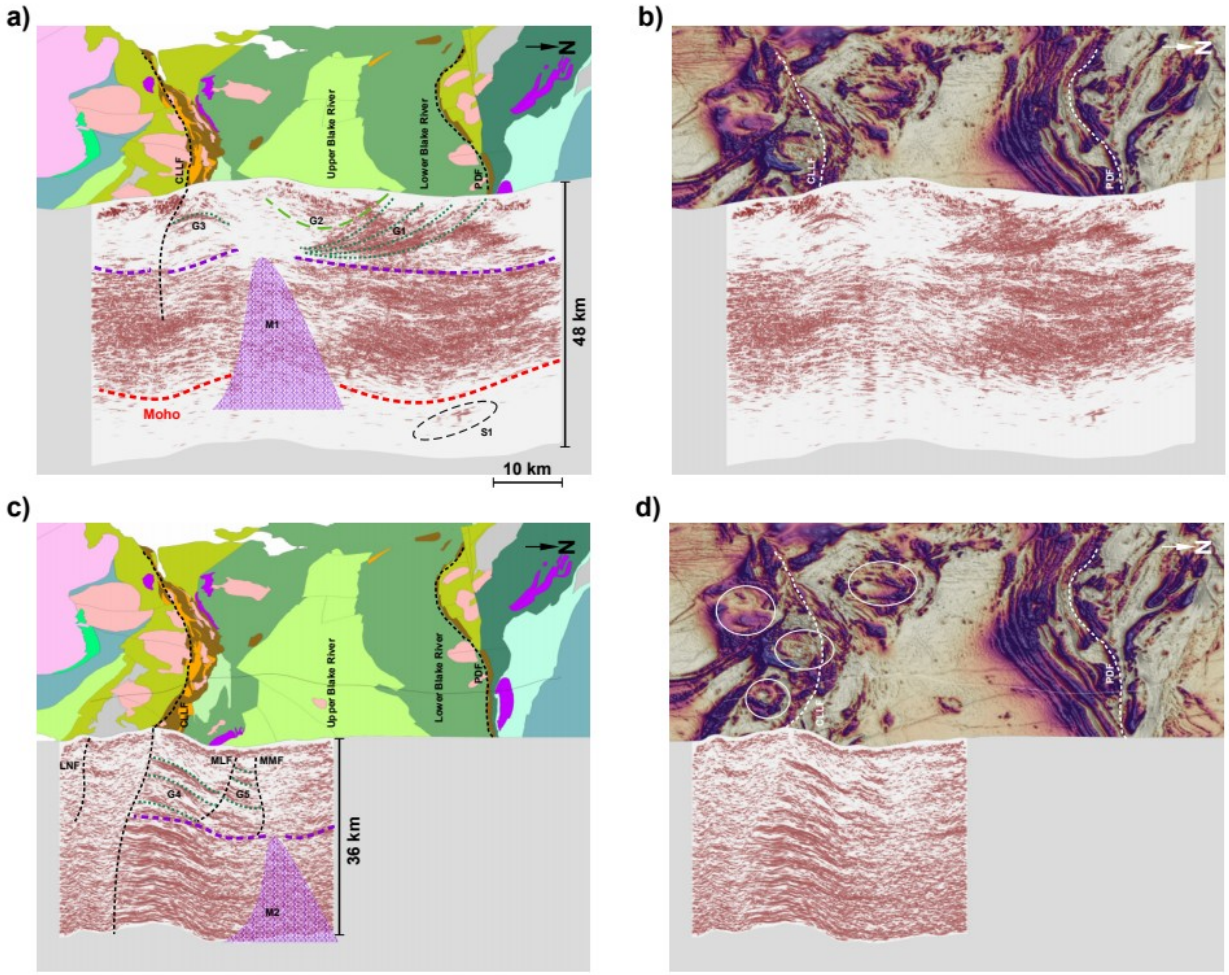

Figure 9: a) and b) show the KSZ12 transect acquired as part of Lithoprobe project overlaid by lithological assemblages and magnetic maps, respectively. c) and d) show the Metal Earth's Larder Lake ME321 transect overlaid by the lithological assemblages and magnetic maps, respectively. The locations of CLLF and PDF were shown on the lithological assemblages map with dashed lines. The white circles in (d) highlight the magnetic responses of syn-tectonic felsic intrusions.

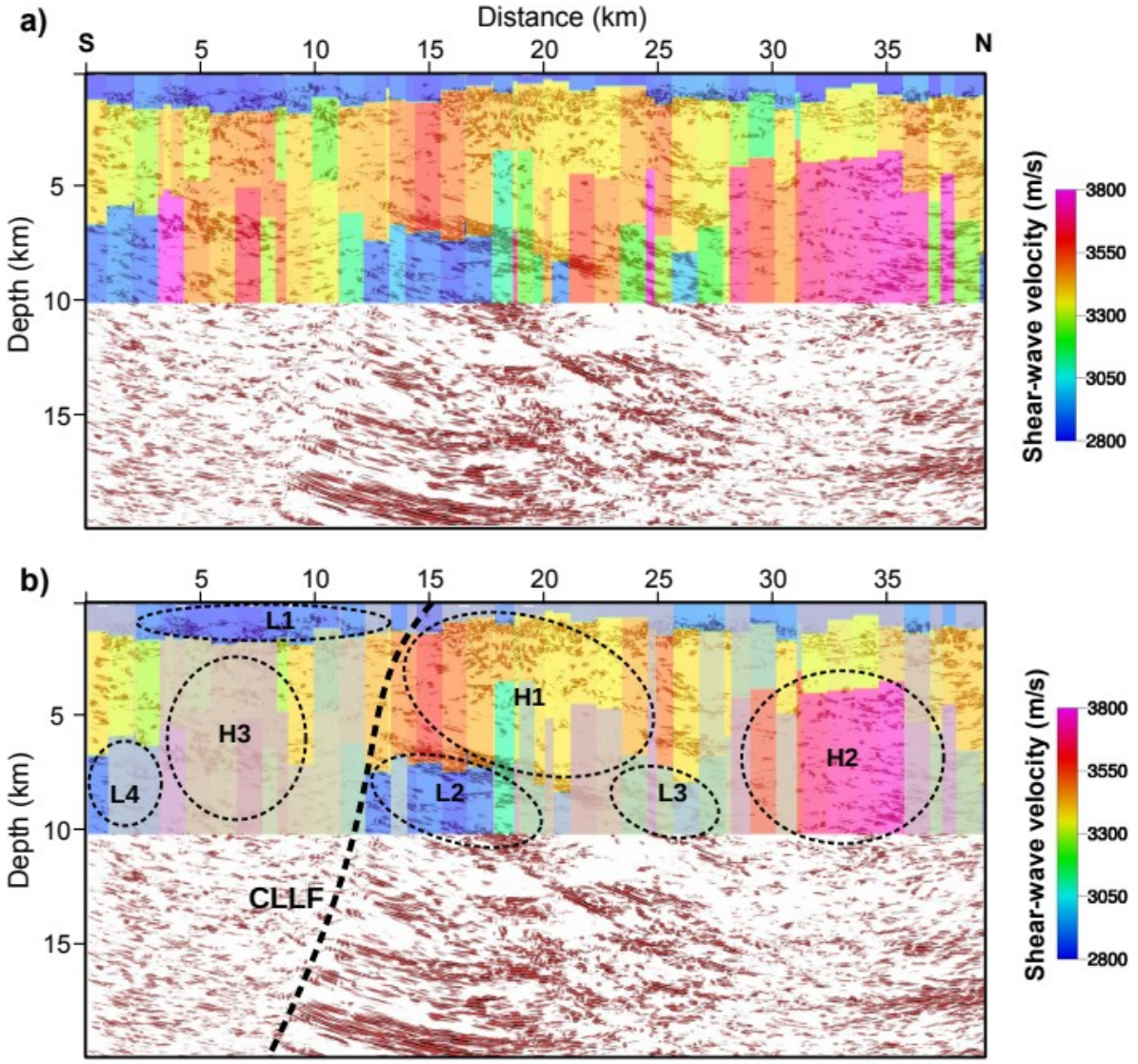

Figure 10: a) The projection of the estimated shear-wave velocity using ANSWT method on the ME321-R1 seismic transect. b) The projection of the shear-wave velocity estimated using ANSWT method on the ME321-R1 seismic transect where parts of the model with an uncertainty of ±50 m/s for the estimated shear-wave velocity were dimmed using a semi-transparent grey tone. The shear-wave anomalies L1, L2, H1, and H2 have a high certainty making them more reliable for geological interpretation purposes.

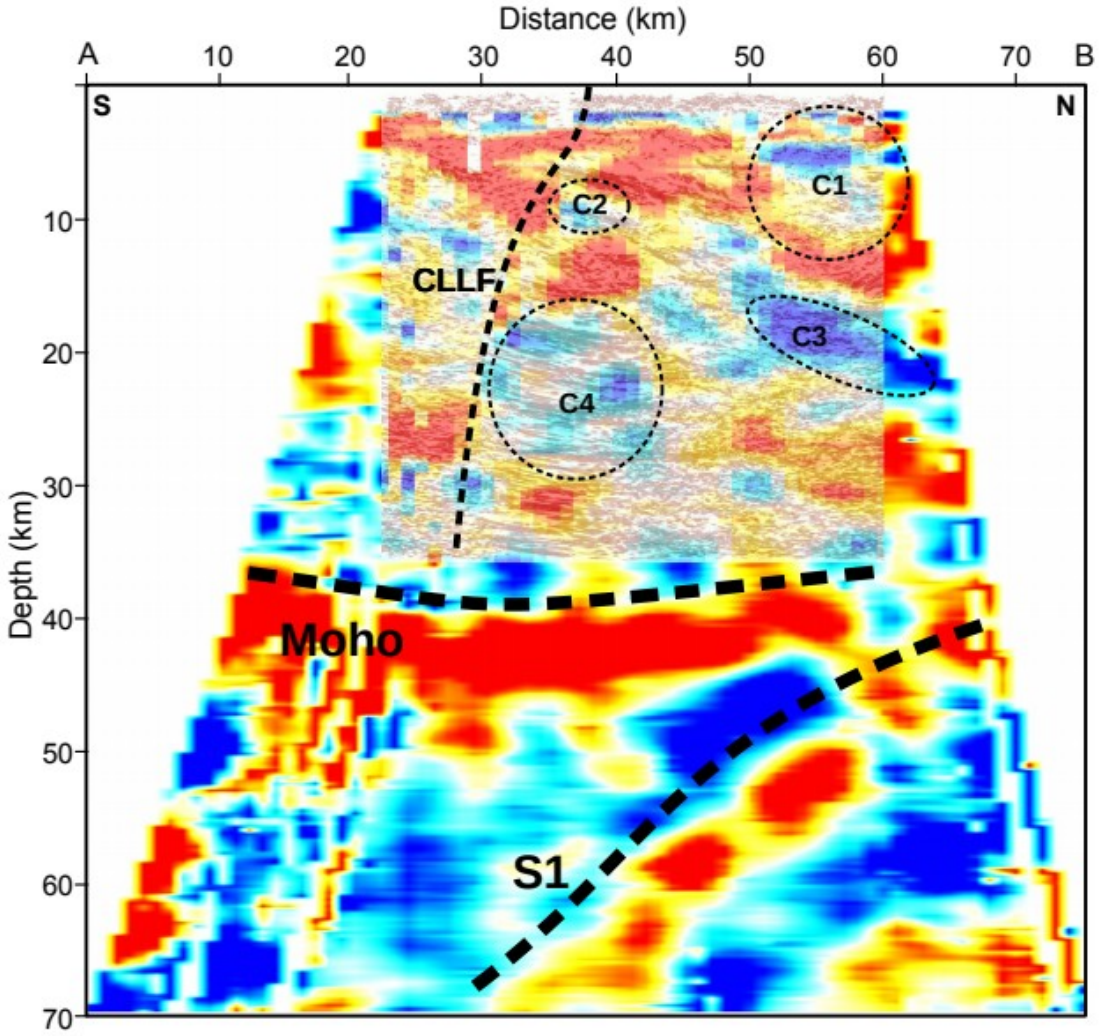

Figure 11: The P-S convertibility profile (the average of all frequency bands) estimated using the receiver function method overlaid on top of the ME321-R1 seismic transect. The colour scale for the convertibility profile is the same as the colour scales in Figure 8. The shallow C1 and C2 anomalies have good correlation with the active seismic and ANSWT model. The C3 anomaly reside on the bottom of upper-crust indicating a significant elastic property change from upper-crust to lower-crust. The C4 anomaly overlies a zone of strong reflections to the north of the CLLF.

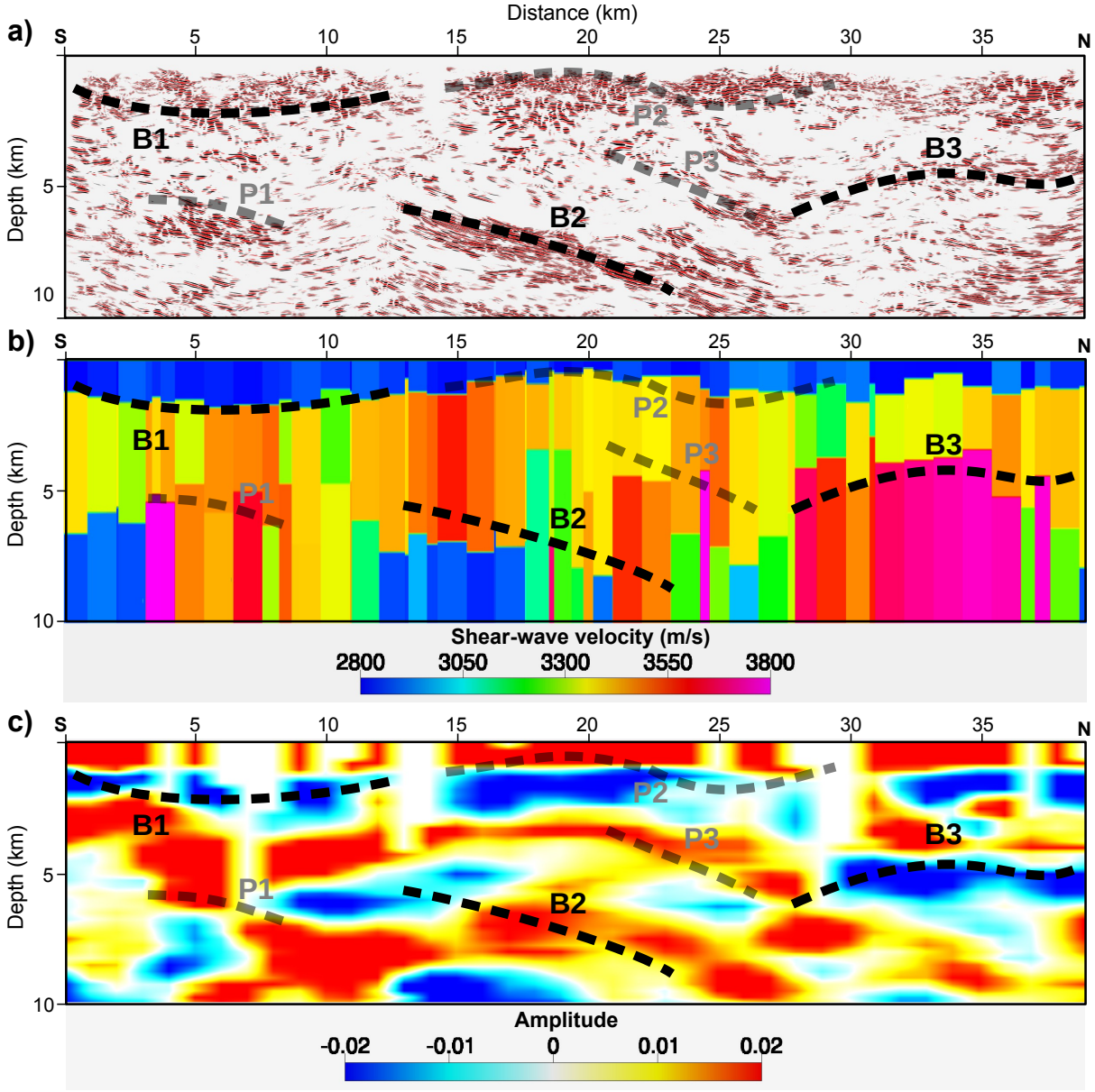

Figure 12: The top 10 km of the a) reflection seismic, b) ANSWT shear-wave velocity, and c) P-S convertibility transects. The B1, B2, and B3 features are highly correlated between all 3 transects. The P1, P2, and P3 features also show noticeable correlation though with low certainty.

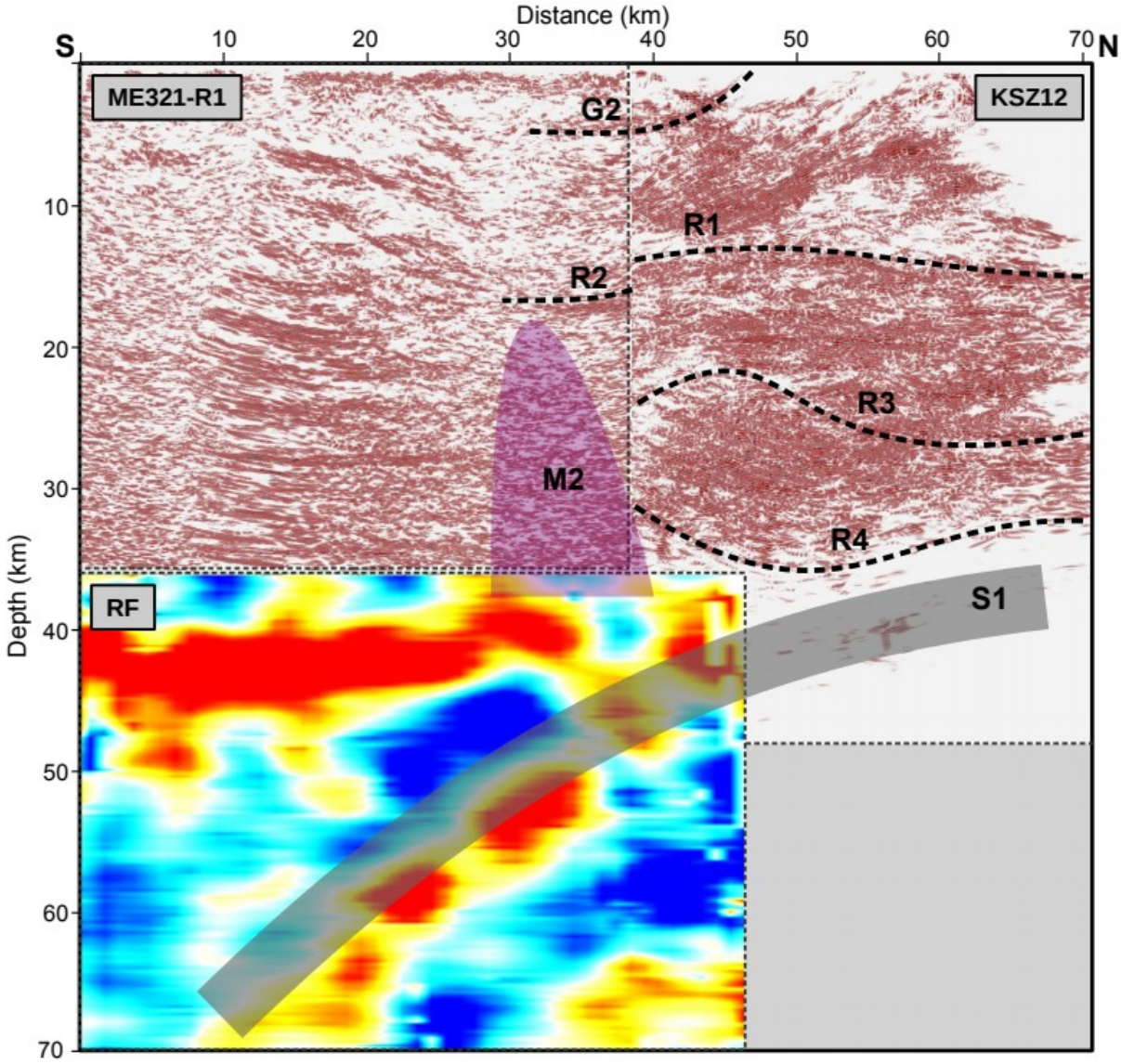

Figure 13: Integrated interpretation of the ME321-R1 and KSZ12 seismic lines and the deeper part of the P-S convertibility transect derived from receiver function analysis. The G2 marks the depth of upper Blake-River volcanic units. The R1 and R2 show the base of the greenstones beneath the KSZ12 and ME321-R1 transects, respectively. The greenstones are 2 to 3 km thicker under the ME321-R1 transect. The S1 slab shows as package of strong reflection below the Moho on the KSZ12 transect and extends to the depth of 70 km (the depth limit of the receiver function analysis). The R3 and R4 mark the bottom of middle-crust and lower-crust regions. The dimmed reflectivity zone, M2, beneath the ME321-R1 similar to the M1 zone beneath the KSZ12 is likely caused by intrusions from the mantle due to the delamination of slab S1.